

Yuri Feldman 

Theoretical analysis of three-dimensional bifurcated flow inside a diagonally lid-driven cavity

Received: 5 October 2014 / Accepted: 28 April 2015 / Published online: 9 May 2015
© Springer-Verlag Berlin Heidelberg 2015

Abstract The instability mechanism of fully three-dimensional, highly separated, shear-driven confined flow inside a diagonally lid-driven cavity was investigated. The analysis was conducted on 100^3 and 200^3 stretched grids by a series of direct numerical simulations utilizing a standard second-order accuracy finite volume code, openFoam. The observed oscillatory instability was found to set in via a subcritical symmetry breaking Hopf bifurcation. Critical values of the Reynolds number $Re_{cr} = 2320$ and the non-dimensional angular oscillating frequency $\omega_{cr} = 0.249$ for the transition from steady to oscillatory flow were accurately determined. An oscillatory regime of the bifurcated flow was analyzed in depth, revealing and characterizing the spontaneous symmetry breaking mechanism. Characteristic spatial patterns of the base flow and the main flow harmonic were determined for the velocity, vorticity and helicity fields. Lagrangian particle tracers were utilized to visualize the mixing phenomenon of the flow from both sides of the diagonal symmetry plane.

Keywords Diagonally lid-driven cavity · Oscillatory instability · Critical Reynolds number Re_{cr} · Critical oscillation frequency ω_{cr} · Spontaneous symmetry breaking · Subcritical Hopf bifurcation

1 Introduction

Investigation of bifurcated shear-driven flows in confined enclosures is important for the understanding major instability mechanisms. The performed studies have included precise determination of critical values of the Reynolds number, Re_{cr} , and of the angular oscillating frequency, ω_{cr} , at which the flow transition to unsteadiness occurs, determination of the character of the bifurcation (supercritical or subcritical) and investigation of the spontaneous symmetry breaking phenomenon. The lid-driven cavity is perhaps the most popular set up traditionally used for modeling confined shear-driven flows. Due to its simple geometry, the incompressible lid-driven cavity flow has been the focus of extensive theoretical and numerical research for many decades. Begun early with theoretical works [1,2] and continued with numerical studies [3,4], state-of-the-art lid-driven flow research covers the entire range of fluid transport phenomena, including longitudinal vortices, corner eddies, non-uniqueness, transition to unsteadiness and turbulence [5].

Today, the two-dimensional lid-driven cavity is a recognized fluid-mechanics benchmark, providing extensive theoretical results for both steady and bifurcated flows [5–7]. However, the two-dimensional flow stability limit is strongly (about 8 times) overstimulated compared with three-dimensional configurations (see, e.g., [8] and [9]). This discrepancy is a result of the complexity of realistic three-dimensional flow, which cannot be explained in terms of its two-dimensional counterpart. Two-dimensional flow results are therefore non-suitable

Communicated by Tim Colonius.

Y. Feldman (✉)

Department of Mechanical Engineering, Ben-Gurion University of the Negev, P.O.B. 653, 84105 Beer-Sheva, Israel
E-mail: yurifeld@bgu.ac.il

for quantitative comparison with the three-dimensional experimental data, and this lack of comparability motivated efforts aimed at conducting linear stability analysis for the three-dimensional flow. The first accurate instability analysis results for three-dimensional lid-driven cavity flow with spatially periodic spanwise boundary conditions were reported by Ding and Kawahara [10]. The results were confirmed and extended in the studies of Albensoeder and Kuhlmann [11] and Theofilis [9], who independently determined the prevalence of the stationary leading mode followed by three different traveling modes. The numerical results obtained by the above authors comprised an important milestone in the investigation of realistic three-dimensional flows, but they could not be straightforwardly verified by experiments. This was because a typical experimental setup has a finite length in the spanwise direction, which necessarily leads to an essentially three-dimensional character of the base flow. For this reason, considerable effort has been put into numerical and experimental investigation of shear-driven flow instability in realistic three-dimensional fully confined enclosures (see eg. [12–14]).

A global instability analysis (with all no-slip boundaries) can in principle be performed either by LU factorization of the Jacobian operator corresponding to a linearized set of Navier-Stokes equations [15] or by providing restricted subsets of the full eigenvector spectrum obtained in a matrix-free form [16,17]. In both approaches, the corresponding eigenproblem is solved by a standard Arnoldi iteration. For complex three-dimensional flows, storage and factorization of the Jacobian operators are prohibitively expensive, which makes the second approach the only viable choice. In this case, the required matrix-vector products are typically provided by time integration of the original or linearized Navier-Stokes equations [18]. Exponential or inverse power methods can then be used to extract the leading eigenvectors of the investigated flow, taking advantage of either in-house developed or available standard CFD time steppers. To the best of our knowledge, the global (with all no-slip boundaries) instability eigenproblem for three-dimensional lid-driven cavity flow was originally solved only by Giannetti et al. [19] and more recently by Gómez et al. [20]. The later group utilized a standard finite volume openFoam package as an integral part of the Arnoldi iteration.

Linear stability analysis is, however, not the ultimate way for the determination of flow instability mechanisms. Feldman and Gelfgat [12] and more recently Kuhlman and Albensoeder [14] successfully utilized a series of direct numerical simulations (DNS) for precise determination of both Re_{cr} and ω_{cr} values. Moreover, conducting a series of DNS for bifurcated flows comprises a convenient way of distinguishing the character of the observed bifurcation (supercritical or subcritical) and of verification of the spontaneous breaking of the flow symmetry [12]. A major advantage of DNS-based analysis is that without a need for the time-consuming Arnoldi iterations whose convergence deteriorates with increasing the grid resolution, it provides a good approximation for the major instability characteristics. It should be noted that the critical value of the oscillating frequency ω_{cr} estimated by DNS can be used as a complex shift for an Arnoldi iteration in the shift-and-invert mode with no need for a time-intensive trial-and-error search if the value is not known a priori.

The main objective of the present study was to demonstrate the potential of DNS conducted with the standard available CFD code openFoam for investigation of the instability of complex, shear-driven and highly separated flows. For this purpose, the flow inside a diagonally lid-driven cavity with the lid moving at 45° to the vertical cavity (see Fig. 1) was chosen. This configuration was first simulated by Povitsky [22–24], who investigated the steady flow characteristics for Re up to 2×10^3 . The diagonally lid-driven cavity essentially hosts a fully three-dimensional, highly separated vortical flow, whose steady state is characterized by a diagonal plane of reflection symmetry. The precise values of the pressure and velocity components of the steady flow along the cavity centerlines at different Re values can be found in [21].

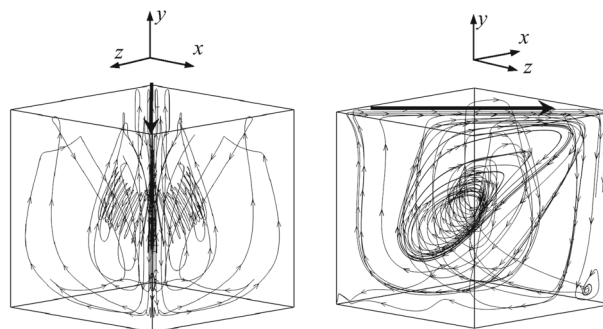


Fig. 1 Flow path lines in a cubic lid-driven cavity whose lid moves at an angle of 45° to the x axis, $Re = 1000$. The arrows indicate the direction of lid movement. Reprinted with permission from [21]

During the past decade, steady diagonally lid-driven flow has become a popular benchmark for verification of state-of-the-art numerical methods [25–28]. Surprisingly, neither the mechanism of transition to unsteadiness nor the classification of the complex bifurcated flow has so far been addressed. The present paper reports on ongoing effort to characterize the oscillatory instability observed for the diagonally lid-driven cavity. The paper focusses on the precise determination of critical Reynolds number Re_{cr} and the angular oscillating frequency ω_{cr} values. It also presents an extended discussion on spontaneous symmetry breaking mechanism of the bifurcated solution, formally proves the subcritical character of the observed Hopf bifurcation, and discusses the main spatial characteristics of the flow instability. The study also includes visualization, based on the Lagrangian particle tracers, demonstrating the mixing phenomenon of the flow from both sides of the diagonal symmetry plane.

2 Computational details and verification

A cubic lid-driven cavity with a side of length L is considered. The top lid of the cavity moves with a constant velocity U at an angle of 45° to the cube's vertical walls (see Fig. 1). All other boundaries of the cavity are stationary. The flow is governed by the incompressible continuity and momentum equations with no-slip boundary conditions applied on all the boundaries:

$$\nabla \cdot \mathbf{u} = 0, \quad (1a)$$

$$\frac{\partial \mathbf{u}}{\partial t} + (\mathbf{u} \cdot \nabla) \mathbf{u} = -\nabla p + \frac{1}{Re} \nabla^2 \mathbf{u}, \quad (1b)$$

where velocity vector $\mathbf{u}(u, v, w)$, pressure p , time t and all length scales are normalized by U , ρU^2 (ρ is the fluid density), L/U and L , respectively. The Reynolds number is defined as $Re = UL/\nu$, where ν is the kinematic viscosity of the fluid. The governing equations (1a and 1b) were solved with the icoFoam solver, which is part of the open-source parallelized code openFoam [29]. Simulations, performed on a standard unix cluster, involved up to 512 cores running in parallel. The SIMPLE algorithm (see, e.g., [30]) was used for pressure–velocity coupling, and a conservative, second-order finite volume scheme was utilized for the spatial discretization in accordance with the openFoam formalism. The time derivative in the momentum equations was approximated by the second-order backward finite difference. An algebraic multigrid algorithm was used for solving iteratively the Navier-Stokes and Poisson pressure correction equations. A maximum value of 10^{-6} for all residuals was set as the convergence criterion. The results from the icoFoam solver were compared with the results previously published by Feldman and Gelfgat [21] for the same flow configuration. Table 1 summarizes the results of the two studies for the velocity and pressure fields obtained for $Re = 1000$ along the vertical centerline of the cavity. Deviations between the corresponding velocity and pressure values did not exceed 1%, thus verifying the present results. Note also that the same values (up to the sixth decimal place) were obtained for the velocity components u_x and u_z , which indicates that the steady-state flow obtained possess reflectional symmetry in agreement with Povitsky [24] and Feldman and Gelfgat [12].

Table 1 Pressure and velocity values along the cavity centerline (0.5, y , 0.5), $Re = 1000$: comparison between the reference [21] (152^3 grid) and the present (100^3 grid) results

y	$u_x, u_z \times 10^3$		$u_y \times 10^3$		$p \times 10^4$	
	Ref.	Pres.	Ref.	Pres.	Ref.	Pres.
0.9766	417.7	417.8	5.378	5.458	51.59	51.42
0.9531	226.6	226.5	16.07	16.14	46.67	46.60
0.8516	76.74	76.39	30.36	30.36	35.18	35.00
0.7344	62.50	62.00	22.59	22.50	21.85	21.73
0.6172	41.78	41.22	5.790	5.561	9.711	9.664
0.5000	−1.398	−1.395	−33.95	−34.08	0.000	0.000
0.4531	−31.54	−31.33	−64.70	−64.35	−2.517	−2.4525
0.2813	−130.7	−129.0	−160.2	−158.0	28.24	28.03
0.1719	−134.7	−133.6	−137.9	−135.9	107.0	106.0
0.1016	−143.1	−142.5	−86.78	−85.41	186.5	184.5
0.0547	−162.2	−161.1	−35.52	−34.49	232.9	230.6

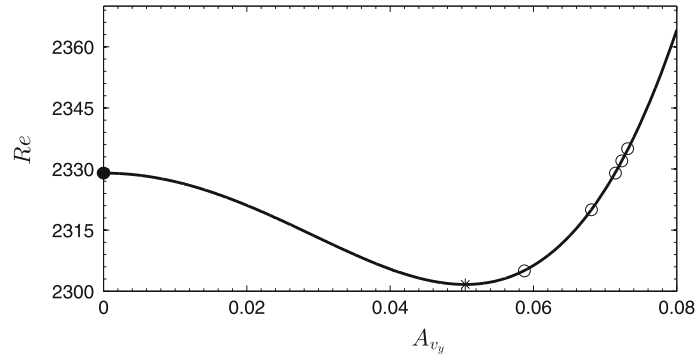


Fig. 2 Values of the amplitude of the u_y component of perturbed flow, monitored at control point $A(0.66, 0.42, 0.56)$ as a function of Reynolds number (marked by *circles*). The trendline was obtained by a least square fit in accordance with Eq. 3. An estimated saddle-node bifurcation point is indicated with an *asterisk*. The linear stability boundary, characterized by a zero amplitude, is distinguished by a *filled circle*

3 Results

3.1 Transition to unsteadiness

The transition to unsteadiness was investigated by simulating the flow just below the critical Reynolds number, Re_{cr} over small increments of Re until at $Re > Re_{cr}$ the steady flow broke down and was superseded by periodic flow motion. Given that this periodic secondary flow is dictated by small amplitude (linear) dynamics, the value of Re_{cr} can be regarded as the Hopf bifurcation point. Mathematically, this means that the spectrum of a linearized set of equations has only a single pair of complex eigenvalues $\sigma \pm i\omega$, whose real part, σ , crosses the axis of neutral stability [31]. In that case, the dynamics of the periodic flow close to the bifurcation point is described by the Hopf theorem [32]:

$$u(t, Re) = u_0(Re_{cr}) + \epsilon \text{Real}(\mathbf{V}e^{i\omega t}) + O(\epsilon^2), \quad \frac{\partial \sigma}{\partial Re} \Big|_{Re_{cr}} \neq 0, \quad (2)$$

where u_0 is the base (steady) flow at $Re = Re_{cr}$, and \mathbf{V} is the leading eigenvector corresponding to the leading eigenvalue $i\omega_{cr}$. If the observed Hopf bifurcation is supercritical, then a stable continuously growing limit cycle exists in the very vicinity of the critical point, and both the oscillation amplitude ϵ and the deviation of the oscillation frequency from its critical value $\omega - \omega_{cr}$ are proportional to $\sqrt{Re - Re_{cr}}$ (see, e.g., [32]). Then, a sequence of ϵ and ω values acquired for two bifurcated flows would provide convenient approximations for Re_{cr} and ω_{cr} .

In contrast, the subcritical bifurcation involves an unstable limit cycle, which cannot be directly reproduced by a time integration close to the bifurcation point. It is distinguished by an abrupt, discontinuous increase in the oscillation amplitude ϵ from zero (at $Re < Re_{cr}$) to some finite value (at $Re > Re_{cr}$). It can also have a hysteresis region that is characterized by different critical Reynolds number values, $Re_{cr1} > Re_{cr2}$, where Re_{cr1} and Re_{cr2} are related to stationary–oscillatory and oscillatory–stationary transitions, respectively. Both of the above characteristics were observed in our numerical simulations. Moreover, applying the Hopf theorem (Eq. 2) to two consequent solutions located on a stable branch of the limit cycle resulted in a considerable (about 10%) underestimation the value of Re_{cr} compared with that tracked by small Re increments. The subcritical type of the observed bifurcation was further verified by a bifurcation diagram obtained for a 100^3 grid by carrying out a series of simulations of bifurcated flow and measuring the amplitudes of the u_y velocity component monitored at control point $A(0.66, 0.42, 0.56)$ as a function of the Reynolds number (see Fig. 2). The specific control point was chosen due to the large values of the u_y oscillation amplitudes observed in its vicinity. The simulations were performed by starting with $Re = 2335$ and proceeding below the predicted Re_{cr} value, to finish with $Re = 2305$.¹ Close to the critical Re_{cr} value, the simulations were carried out by using small $\Delta Re = 3$ decrements. In each case, the equilibrium amplitude was verified by measuring the same value (up to the fourth decimal place) for at least the 30 last periods. To reduce computational times, asymptotic

¹ The procedure for determining the critical value of the Reynolds number, Re_{cr} , is detailed in the two last paragraphs of the section

pressure and velocity fields obtained for a specific Re were then used as initial condition for performing the simulation with the subsequent Re value.

Following the recent work of Kuhlmann and Albensoeder [14], the bifurcation diagram was obtained according to

$$Re - Re_{cr} = -a_0 A^2 + a_1 A^4, \quad (3)$$

with $a_0 = 2.146 \times 10^4$ and $a_1 = 4.211 \times 10^6$, where the saddle-node bifurcation point $Re_* \approx 2302$ is denoted by an asterisk. The hysteresis depth is equal to $\Delta Re = Re_{cr} - Re_* = 27$, comprising 1.16% of Re_{cr} . The estimated Re_* value was consistent with the results obtained by simulating the flow with $Re = 2300 < Re_*$ (not shown here) and exhibiting a qualitatively different, typical of subcritical flow trend characterized by an exponential decay of all the velocity components to their steady-state values.

Adapting an approach recently applied by Feldman and Gelfgat [12], the critical values were estimated by analyzing a time series corresponding to the flow regimes simulated for a Reynolds number just below the value of Re_{cr} and characterized by decaying oscillation amplitudes. The approach is based on the observation that, after a sufficiently long time, the subcritical flow close to the bifurcation point is dictated only by the most unstable mode, while the flow oscillations $f(t)$ decay proportionally to $e^{\sigma + i\omega t}$, $\sigma < 0$, and the value of σ is calculated by:

$$\sigma = \frac{\ln(f(t_k)/f(t_{k-1}))}{t_k - t_{k-1}}, \quad (4)$$

where t_k ($k = 1, 2, 3, \dots$) corresponds to the instantaneous times when the flow oscillations $f(t_k)$ attain their local maxima. The values of Re_{cr} and ω_{cr} are then calculated by extrapolation of σ to zero. Time evaluations of the u_x component of the velocity monitored for the values of $Re = 2300$ and $Re = 2325$ within the region with the largest oscillation amplitudes (control point $A(0.66, 0.42, 0.56)$) are shown in Fig. 3. As expected, a lower decay ratio corresponds to the higher Re , which was chosen to be very close to the bifurcation point.

The same calculations were repeated for a refined grid containing 200^3 finite volumes. The critical values calculated for the two grid resolutions are given in Table 2. For all cases, the values of σ and ω were calculated by basing on at least ten different pairs of the local maxima and verified up to the third decimal place. We also used Fourier analysis (not shown here) to verify that the frequency spectrum of all the signals contains only a single value corresponding to a leading mode, while the disturbances introduced by other modes have already adequately decayed. Following the works of Feldman and Gelfgat [12] and Gelfgat [17], the Richardson

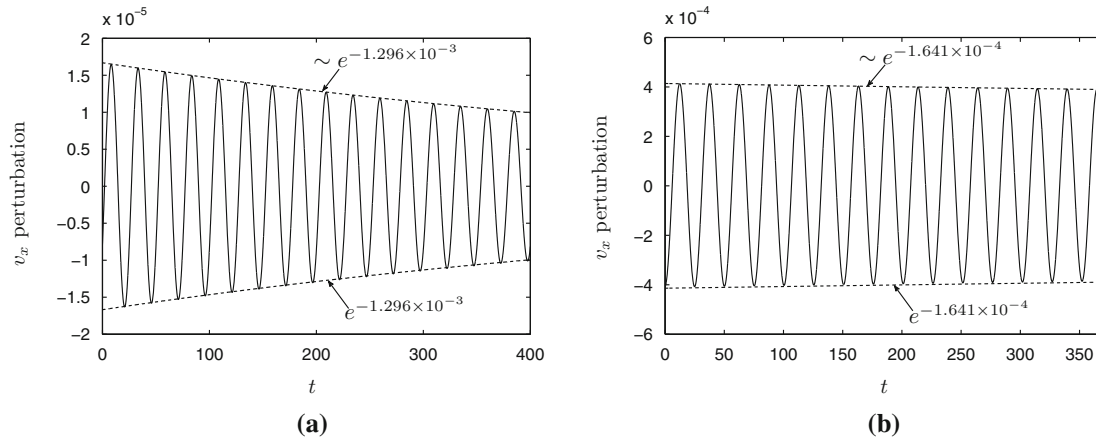


Fig. 3 Time evaluation of the u_x velocity component monitored at a control point $A(0.66, 0.42, 0.56)$, 100^3 grid: **a** $Re = 2300$; **b** $Re = 2325$

Table 2 Estimation of Re_{cr} and ω_{cr} values

Grid resolution	Re_{cr}	ω_{cr}
100^3	2329	0.2495
200^3	2321	0.2488
Richardson extrapolation	2320	0.249

Highest precision values are in bold

extrapolation was applied to further improve the grid-dependent Re_{cr} and ω_{cr} results to their zero-grid-size asymptotic values, yielding $Re_{cr} = 2320$ and $\omega_{cr} = 0.249$ values.

3.2 Global and local characteristics of the steady flow

To verify the value of the critical Reynolds number, simulations for $Re = 2310 < Re_{cr}$ were performed, taking the steady flow obtained for $Re = 2300$ as the initial condition. As expected, the results showed a rapid convergence to the steady-state solution, similar to that previously observed for the $Re = 2300$ (see Fig. 3a). The steady-state flow patterns shown in Fig. 4 were calculated by time averaging of the decaying velocities at each point of the computational domain over fifty periods. We next define a new right-handed cartesian coordinate system $X'(X', Y', Z')$ “naturally” associated with the direction of the flow: The X' axis coincides with the direction of lid motion, the Y' axis is the same as Y , and the Z' axis is perpendicular to the diagonal plane of the cavity. In the new coordinate system, the velocity components u_{dir} and u_{perp} in the X' and Z' directions, respectively, are obtained by projections of the u_x and u_z velocity components as follows:

$$u_{dir} = (u_z + u_x)\sqrt{2}/2, \quad (5a)$$

$$u_{perp} = (u_z - u_x)\sqrt{2}/2. \quad (5b)$$

As can be seen from Fig. 4a and b, the flow driven by the lid motion recirculates inside the cavity in the clockwise direction. The spatial distribution of both \bar{u}_{dir} and \bar{u}_{ver} components is symmetric relative to the main diagonal plane. In contrast, the spatial distribution of the \bar{u}_{perp} component is antisymmetric, and its values are equal to zero on the plane itself. The values of the \bar{u}_x , \bar{u}_y and \bar{u}_z velocity components along the horizontal ($x = z, 0.5, z = x$) and vertical ($0.5, y, 0.5$) centerlines are given in Table 3. For both centerlines, it was verified that the values of \bar{u}_x and \bar{u}_z are equal up to the fifth decimal place, verifying the flow symmetry relative to the diagonal plane.

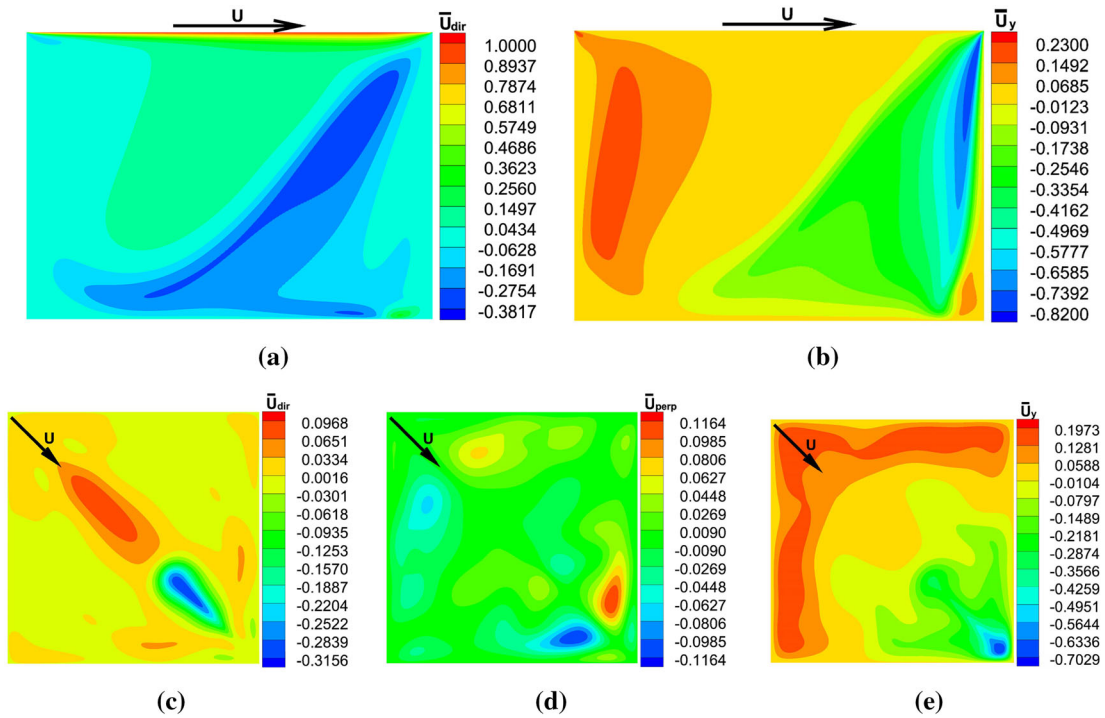


Fig. 4 Distribution of the steady-state velocity components obtained for $Re = 2310$ on a 200^3 grid. The arrows indicate the direction of the lid movement: **a** \bar{u}_{dir} velocity component in the main diagonal plane; **b** \bar{u}_y velocity component in the main diagonal plane; **c** \bar{u}_{dir} velocity component in the span midplane; **d** \bar{u}_{perp} velocity component in the span midplane; **e** \bar{u}_y velocity component in the span midplane

Table 3 Values of the steady flow velocity components along the cavity centerlines (0.5, y , 0.5) and ($x = z$, 0.5, $z = x$) obtained for $Re = 2310$ on a 200^3 grid

$y(x = z = 0.5)$	$\bar{u}_x, \bar{u}_z \times 10^3$	$\bar{u}_y \times 10^3$	$x, z(y = 0.5)$	$\bar{u}_x, \bar{u}_z \times 10^3$	$\bar{u}_y \times 10^3$
0.9766	303.6	8.370	0.6906	-221.9	-292.0
0.9531	130.1	19.74	0.6739	-299.9	-217.1
0.8516	82.64	17.67	0.6022	-14.41	-53.06
0.7344	75.23	14.44	0.5193	43.66	15.16
0.5000	48.21	19.26	0.3536	68.29	43.14
0.4531	41.59	16.12	0.3204	66.30	51.35
0.2813	-152.7	-193.5	0.1989	22.77	111.1
0.1719	-169.0	-173.4	0.1216	6.518	174.4
0.1016	-136.0	-119.5	0.0718	6.637	191.4
0.0547	-126.8	-63.51	0.0387	5.365	102.5

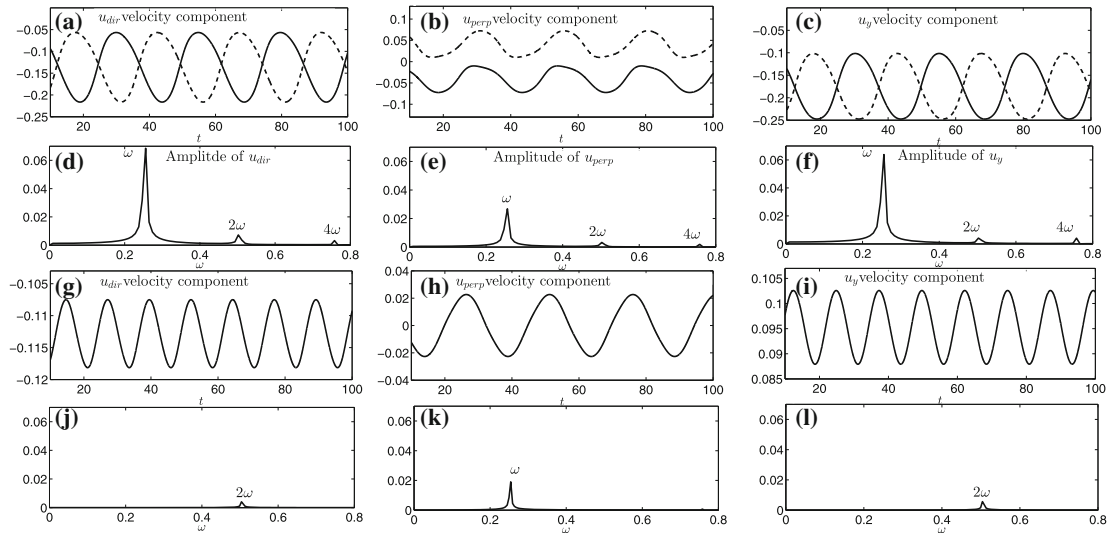


Fig. 5 Time evaluations of the u_{dir} , u_{perp} , and u_y velocity components and the corresponding frequency spectra, $Re = 2335$: **a-f** solid line—control point A(0.66, 0.42, 0.56), dashed line—control point B(0.56, 0.42, 0.66); **g-l** control point C(0.1, 0.14, 0.1)

Table 4 Maximum and minimum values of the velocity components monitored for $Re = 2325$ (bifurcated flow) at control points A(0.66, 0.42, 0.56), B(0.56, 0.42, 0.66) and C(0.1, 0.14, 0.1)

	Control points A and B		Control point C	
	max	min	max	min
u_{dir}	-0.5667	-0.2164	-0.1075	-0.1181
u_{perp}	0.07237	0.010026	0.02266	-0.02266
u_y	-0.1015	-0.2474	0.1026	0.08791

3.3 Bifurcated flow: monitoring discrete control points

A bifurcated oscillatory flow field in the very vicinity of the subcritical Hopf bifurcation point, $Re = 2335$ ($Re > Re_{cr}$), is considered. After a sufficiently long time, the spectrum of this flow consists solely of a single frequency value (and its multipliers caused by nonlinear effects) corresponding to the unstable mode, while all the disturbances initially introduced into the system are damped to the machine zero [12]. This is true for every flow property monitored at any internal point of the confined volume. Figure 5 shows the time evaluations and the corresponding frequency spectra of the u_{dir} and u_{perp} and u_y components monitored at three control points: a pair of reflectional symmetric points A(0.66, 0.42, 0.56) and B(0.56, 0.42, 0.66) with respect to the main diagonal plane of the cavity and point C(0.1, 0.14, 0.1) independently chosen on the main diagonal plane. The maximum and minimum values of the velocity components monitored for $Re = 2325$ (bifurcated flow) at the control points A(0.66, 0.42, 0.56) and B(0.56, 0.42, 0.66) symmetrically located from both sides of the main diagonal plane and at the control point C(0.1, 0.14, 0.1) located on the main diagonal plane are detailed in

Table 4. Note that instantaneous values of the u_{perp} velocity component at the control point C are not equal to zero, in contrast to its mean value ($\max(u_{\text{perp}}) = -\min(u_{\text{perp}})$), see Table 4).

Signals monitored in a pair of reflectional symmetric points A and B (see Fig. 5a–c) are characterized by the same u_{dir} and u_y and by the opposite u_{perp} mean velocity values, respectively. Their spectra (see Fig. 5d–f) contain the frequency of the main harmonic and its multipliers caused by nonlinear flow dynamics. Given an arbitrary choice of all three control points, the observations made can be explained by the global reflectional symmetry of the bifurcated flow base velocity $\bar{\mathbf{u}}(X')$ with respect to the main diagonal plane, $K_{X'}\bar{\mathbf{u}}(X') = \bar{\mathbf{u}}(X')$, where the spatial reflection $K_{X'}$ reads: $X' \rightarrow X'$, $\bar{u}_{X'} = \bar{u}_{X'}$; $Y' \rightarrow Y'$, $\bar{u}_{Y'} = \bar{u}_{Y'}$; $Z' \rightarrow -Z'$, $\bar{u}_{Z'} = -\bar{u}_{Z'}$. The spatial reflection symmetry of the base velocity of perturbed flow originates from that of the steady flow reported by [21,24] and preserves during transition to unsteadiness. In contrast, transition to unsteadiness of the “classical” lid-driven cavity flow is characterized by the symmetry breaking of the base flow [12] with the subsequent energy bursts of the bifurcated flow [14]. It is clear that the instantaneous velocity fields monitored at symmetric points A and B are equal (or with the opposite sign for the transverse component) half a period apart, up to a small temporal offset persisting in all the signals (see Fig. 5a–c). The offset observed is critical for understanding the symmetry breaking Hopf bifurcation and the symmetries of the bifurcated solution. Without an offset, a bifurcated periodic solution would be invariant under the action of spatiotemporal symmetry H half a period apart, preserving the Z_2 symmetry group [33] and formally reading:

$$Hu(X', t) = K_{Z'}(X, t + T/2) = (u_{X'}, u_{Y'}, -u_{Z'})(X', Y', -Z', t + T/2), \quad (6)$$

with H -symmetric base flow $H\bar{\mathbf{u}}'(X') = K_{Z'}\bar{\mathbf{u}}'(X')$, where $K_{Z'}$ is the spatial reflection: $Z' \rightarrow -Z'$, $u_{Z'} \rightarrow -u_{Z'}$ and T is period of the perturbed flow oscillations dynamically determined by the corresponding Re number. A representative example of this symmetry is the von Karman street wake, whose symmetries are discussed in detail in [34,35]. The existence of the offset, however, alters the above scenario, since in that case, the bifurcated velocities monitored from both sides of the symmetry plane are not precisely half a period apart. To clarify whether the offset observed has a physical origin or is simply a consequence of the nonlinear dynamics of the system, we draw the reader’s attention both to the time evaluations of the velocity components acquired at point C in the diagonal plane (see Fig. 5g–i) and to the corresponding frequency spectra (see Fig. 5j–l). One can clearly recognize two main differences when the signals monitored at points A and B are compared with those acquired at point C . First, at points A and B , the oscillation amplitudes of all three velocity components are of the same order of magnitude, whereas at point C , the amplitude of the u_{perp} velocity is an order of magnitude higher than the corresponding values of the u_{dir} and u_y velocities. Second, the main harmonic existing in all three velocity components at points A and B is persistent only in the u_{perp} component at point C , whereas the u_{dir} and u_y signals contain only the second harmonic characterized by twice the frequency (see Fig. 5j–k). This difference arises because the offset between the time evaluations of the u_{dir} and u_y velocity components monitored at any pair of reflectional symmetric points tends to zero as the distance between the points and the cavity diagonal plane decreases. In the diagonal plane, the u_{dir} and u_y velocity components are precisely half a period apart and therefore cancel each other out. The offset between time evaluations of all the velocity components acquired at the reflectional symmetric points is a direct consequence of the nonzero periodic u_{perp} velocity in the diagonal plane, which is inherent in perturbed flow. The observed spatiotemporal symmetry breaking can therefore be attributed to the three-dimensional character of the perturbed flow throughout the cavity (including the diagonal plane) which—in contrast to two-dimensional symmetric type-periodic flows (see, e.g., [34,35])—is not invariant under a reflection plus a half period advance in time and does not preserve Z_2 space-time symmetry after undergoing Hopf bifurcation.

3.4 Bifurcated flow: spatial characteristics

The qualitative characteristics of the bifurcated flow discussed in the previous section are based on the data acquired at only three discrete points and therefore require supplemental generalization. This section investigates the spatial distribution of the main characteristics of bifurcated flow. We start by presenting the flow oscillation amplitudes for all three velocity components calculated for the periodic, fully developed flow ($Re = 2335$) determined by only a single oscillating mode. The analysis was performed by computing the deviation between the maximum and the base flow values of a given velocity component attained at each grid point and averaged over several oscillation periods. Next, we plotted isosurfaces confining the regions where the averaged oscillation amplitudes are no <25% of the maximal amplitude of the corresponding velocity component, as shown in Fig. 6a–c. The contours of the maximal averaged amplitudes in the spanwise and main diagonal cross

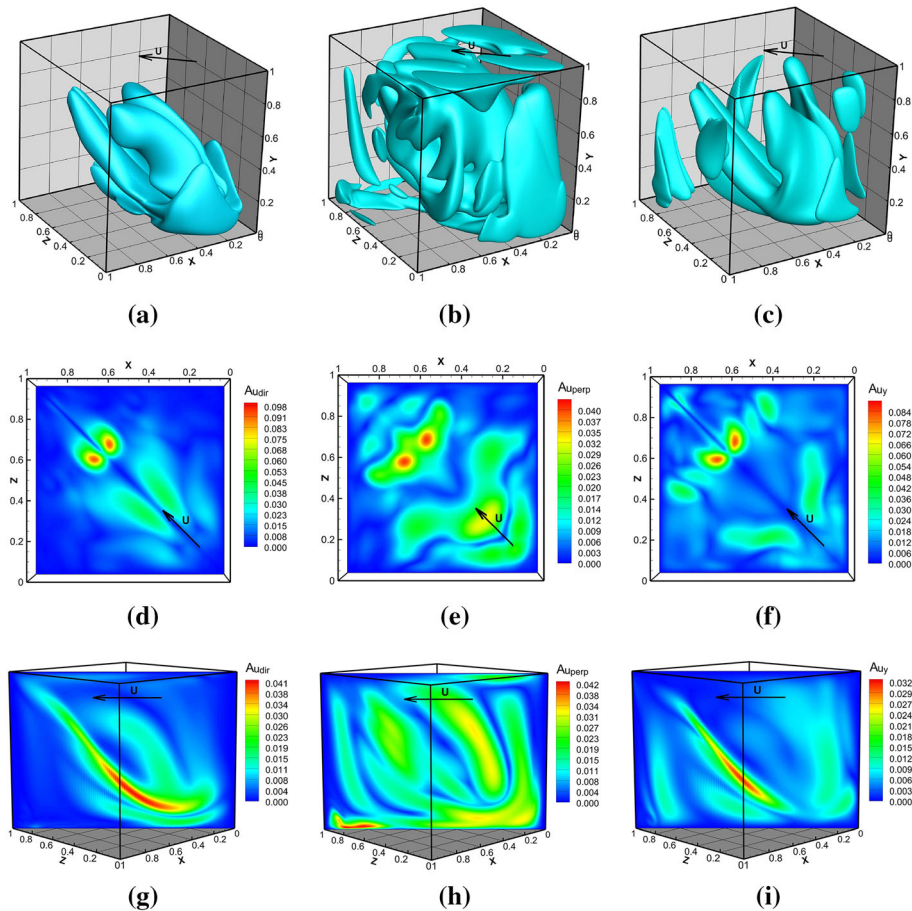


Fig. 6 Spatial distribution of the oscillation averaged amplitudes for the u_{dir} , u_{perp} , and u_y velocity components, $Re = 2335$. The *arrows* indicate the direction of lid movement: **a–c** three-dimensional contours confining the areas with $A \geq 0.25A_{max}$; **d–f** values obtained in the horizontal midplane; **h–j** values obtained in the main diagonal cross section

sections are shown in Fig. 6d–f and g–i, respectively. The procedure constitutes a convenient way to determine the most energetic flow regions (see, e.g., [36] and [12]). It should be noted that because of the subcritical character of the bifurcation, the calculated averaged oscillation amplitudes cannot be formally related to the absolute values of the flow eigenvectors. Nevertheless, given the good agreement between the previous DNS study [12] (on the “classical” lid-driven cavity) and the corresponding formal linear stability analysis [19,20], one can expect a striking resemblance between the spatial patterns of both flow characteristics.

As can be easily recognized, the spatial pattern of the amplitudes is reflectional symmetric with respect to the main diagonal plane of the cavity. The maximum values of all the oscillation amplitudes are side biased from the main diagonal surface. At the same time, there are substantial qualitative differences between the spatial distributions of the directional and vertical amplitudes $A_{u_{dir}}$ and A_{u_y} , respectively, compared with the spatial distribution of the perpendicular amplitude $A_{u_{perp}}$. First, $A_{u_{dir}}$ and A_{u_y} are compactly grouped around the main diagonal plane, while $A_{u_{perp}}$ is widely dispersed and occupies the bulk of the cavity volume (see Fig. 6a–c). Second, the maxima of $A_{u_{dir}}$ and A_{u_y} are about twice the maximum of $A_{u_{perp}}$ (Fig. 6d–f). Third, the maximal values of the $A_{u_{dir}}$ and A_{u_y} oscillation amplitudes observed on the spanwise cross-sectional plane are more than twice those found on the main diagonal plane, while the values of $A_{u_{perp}}$ are about the same on both planes. The observed differences indicate that u_{dir} and u_y oscillations are prevalent in the dynamics of the developed bifurcated flow.

Providing useful information about the character of the observed oscillatory instability, the flow oscillation amplitudes are still affected by the existence of the main harmonic multipliers (due to the flow nonlinearity), and therefore, they cannot entirely address the spatial characteristics of the unstable oscillatory mode. Further processing is required to filter out the nonlinear effects, which is achieved by performing a Fourier

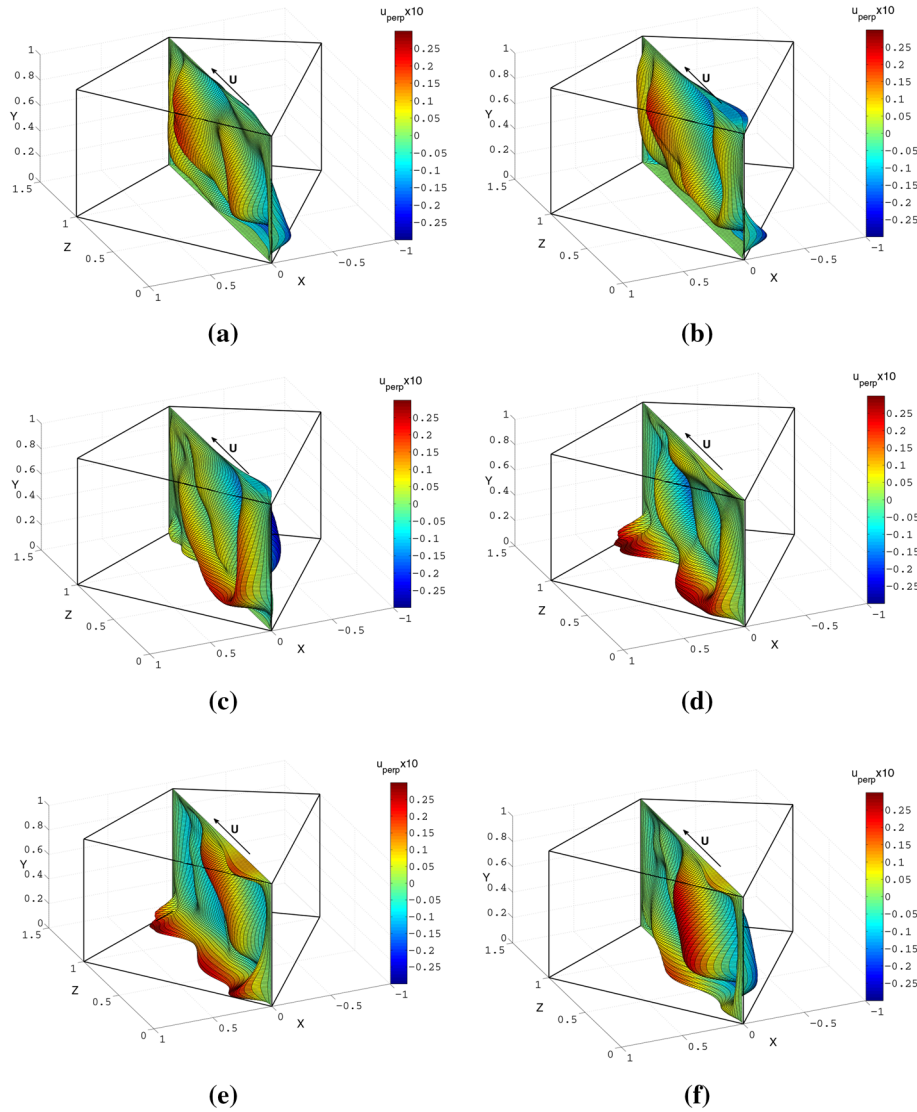


Fig. 7 Spatial distribution of $u_{\text{perp}} \times 10$ perturbation in the diagonal plane of symmetry for $t = [T/6, T/3, T/2, 2T/3, 5T/6, T]$, $Re = 2335$. The arrows indicate the direction of lid movement

transform of the flow and applying a standard band-pass filter. The filtered flow velocity $\mathbf{u}(\mathbf{x}, t)$ containing only the main harmonic (without its multipliers) superimposed upon the velocity base flow $\mathbf{u}_m(\mathbf{x})$ can then be straightforwardly reconstructed by the inverse Fourier transform:

$$\mathbf{u}(\mathbf{x}, t) = \mathbf{u}_m(\mathbf{x}) + \mathbf{a}(\mathbf{x}) \cos(\omega t) + \mathbf{b}(\mathbf{x}) \sin(\omega t) \quad (7)$$

where \mathbf{a} and \mathbf{b} are Fourier coefficients, and \mathbf{x} is a spatial coordinate vector. As has already been mentioned, the symmetry breaking observed in the oscillatory regime is directly related to a nonzero value of the instantaneous velocity component u_{perp} that is perpendicular to the cavity diagonal plane of symmetry. A better visualization of the symmetry breaking mechanism can be achieved by representing an instantaneous pattern of the main u_{perp} harmonic reconstructed for the diagonal plane of symmetry of the cavity. The perturbation multiplied by a factor of ten $10 \times u_{\text{perp}}$ (for visualization purposes) is shown in Fig. 7 for six discrete times spread evenly over the flow oscillating period.

The images in Fig. 7 can be thought of as showing a deflection that will experience an imaginary massless shell with infinitely small stiffness if positioned in the diagonal plane of symmetry and subjected exclusively to a perturbation (without the base flow) of the supercritical regime discussed. Clearly, the temporal distribution obtained is consistent with the spatial distribution corresponding to the u_{perp} oscillation amplitudes in the

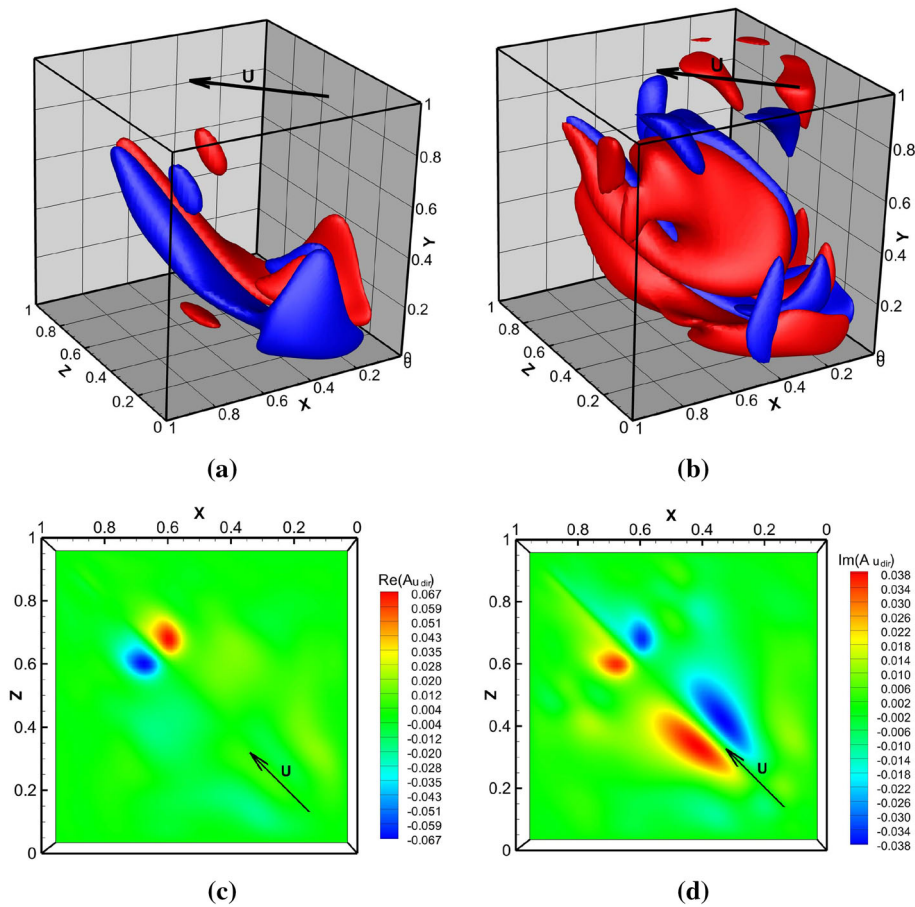


Fig. 8 The spatial distribution of the real and imaginary parts of the u_{dir} main oscillating mode with the corresponding spanwise cross section ($y = 0.5$). The lid moves as indicated by the *arrows*, $Re = 2335$: **a, c** three-dimensional contours confining the areas with $|Re(A_{u_{\text{dir}}})| \geq 0.25 \times \max(|Re(A_{u_{\text{dir}}})|)$; **b, d** three-dimensional contours confining the areas with $|Im(A_{u_{\text{dir}}})| \geq 0.25 \times \max(|Im(A_{u_{\text{dir}}})|)$

diagonal plane of symmetry of the cavity (see Fig. 6h). In both figures, the trailing bottom corner of the cavity is characterized as a region with the maximal values of u_{perp} oscillation amplitudes.

Further generalization of the oscillatory mode is due to the spatial distributions of the real and imaginary parts of the main harmonic provided by a Fourier transform (performed at every point of the computational domain for all three velocity components). It was verified that over the entire computational domain, the main harmonic perturbation (both real and imaginary parts of the corresponding Fourier transform) is fully antisymmetric (identical up to a sign) in terms of the u_{dir} and u_y velocity components (see Figs. 8, 10) and fully reflective symmetric (identical) with regard to the u_{perp} velocity component (see Fig. 9).

The finding that the main harmonic components u_{dir} and u_y are antisymmetric infers their zero values on the diagonal plane in contrast to the main harmonic of u_{perp} , which exists over the entire diagonal plane. This fact is in line with the observations of the previous section, revealing the existence of the main harmonic only in the signal corresponding to the u_{perp} velocity component, monitored at point C (see Fig. 5j–l). In summary, on the symmetry plane and in its near vicinity, oscillations of the bifurcated flow are dominated by the main u_{perp} velocity harmonic, which is characterized by a reflectional symmetry spatial distribution. In contrast, the flow oscillations far from the symmetry plane are determined by the antisymmetric u_{dir} and u_y and the symmetric u_{perp} harmonics, that in turn affect out-of-phase u_{dir} and u_y and in-phase u_{perp} velocity oscillations, respectively, relative to the main diagonal plane.

The mechanism above described of spontaneous spatiotemporal symmetry breaking due the presence of nonzero u_{perp} oscillations over the entire diagonal plane of symmetry superimposed on reflectional symmetric base flow may also be verified by analyzing the flow helicity. This quantity, defined as the volume-integrated scalar product of the velocity field $\mathbf{u}(\mathbf{x}, t)$ and the vorticity field $\boldsymbol{\omega}(\mathbf{x}, t) = \text{curl } \mathbf{u}$, is of key importance in

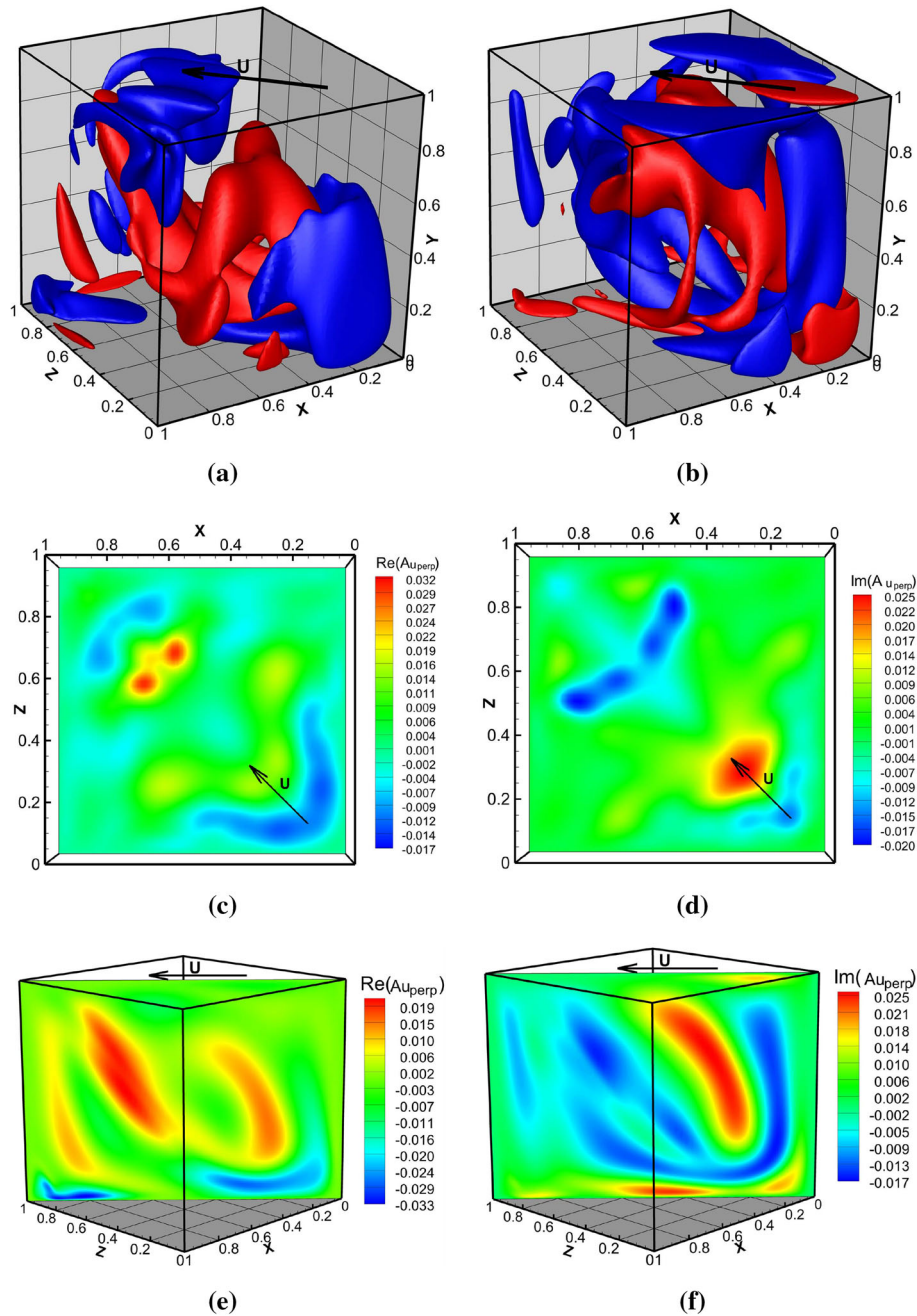


Fig. 9 The spatial distribution of the real and imaginary parts of the u_{perp} main oscillating mode with the corresponding spanwise cross section ($y = 0.5$). The *arrows* indicate the direction of lid movement, $Re = 2335$; **a, c** three-dimensional contours confining the areas with $|Re(A_{u_{\text{perp}}})| \geq 0.25 \times \max(|Re(A_{u_{\text{perp}}})|)$; **b, d** three-dimensional contours confining the areas with $|Im(A_{u_{\text{perp}}})| \geq 0.25 \times \max(|Im(A_{u_{\text{perp}}})|)$

the characterization of the reflectional symmetry (or lack thereof) of a fluid flow [37–40]. When looking at the spatial characteristics of turbulent flow, it is convenient to introduce the helicity density as a scalar field defined by $h(\mathbf{x}, t) = \mathbf{u}(\mathbf{x}, t) \cdot \boldsymbol{\omega}(\mathbf{x}, t)$ and to calculate it in terms of the base flow and the whole flow spectrum [41]. In this section, we focus on investigating the base flow and the main harmonic helicity densities. If the flow is reflectional symmetric, both fields will vanish on the symmetry plane [38]. Figure 11 shows the spatial distributions of helicity densities corresponding to the base flow (Fig. 11a) and to the real (Fig. 11b) and imaginary (Fig. 11c) parts of the main flow harmonic taken at the mid-span cross section of the cavity.

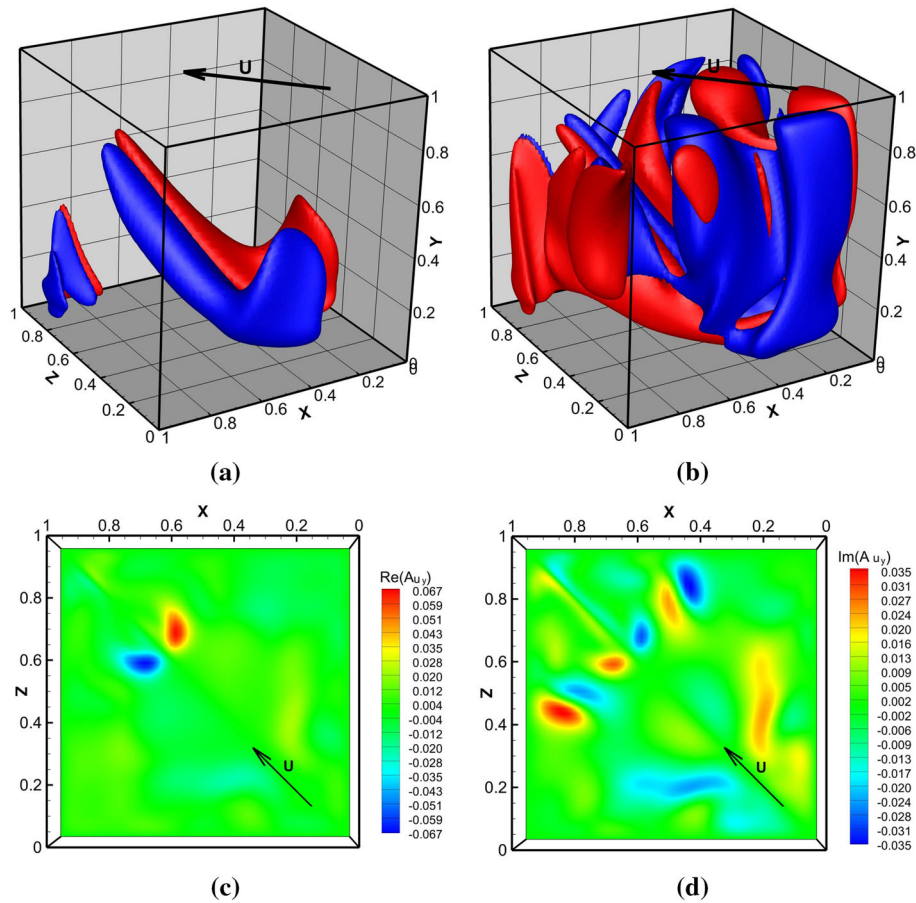


Fig. 10 The spatial distribution of the real and imaginary parts of the u_y main oscillating mode with the corresponding spanwise cross section ($y = 0.5$). The *arrows* indicate the direction of lid movement. **a, c** three-dimensional contours confining the areas with $|Re(A_{u_y})| \geq 0.25 \times \max(|Re(A_{u_y})|)$; **b, d** three-dimensional contours confining the areas with $|Im(A_{u_y})| \geq 0.25 \times \max(|Im(A_{u_y})|)$

It can be seen that the helicity density of the base flow is antisymmetric, while the main harmonic helicity densities are reflective symmetric relative to the diagonal symmetry plane. As expected, the base flow helicity density vanishes on the symmetry plane, thus verifying its reflectional symmetry. In contrast, both the real and the imaginary parts of the main harmonic helicity density have nonzero symmetry plane values, indicating reflectional symmetry breaking of the bifurcated flow. The presence of nonzero u_{perp} oscillations on the symmetry plane can also be visualized by following Lagrangian tracers with initial symmetric distribution in the vicinity of the symmetry plane. Figure 12 shows the temporal evaluation of the tracers for $t = T/5, T/4,$ and $T/3$, where T is the oscillation period corresponding to the main harmonic. It is remarkable that no mixing is observed between the particles from the two sides of the symmetry plane when those particles are exposed only to the base flow (see Fig. 12a, d, g). One can clearly recognize interosculation of the particles from the two sides of the cavity midplane exposed to the oscillatory flow determined only by the main harmonic (without base flow, see Fig. 12b, e, h). In the absence of base flow, particle interosculation progresses continuously with time, occurring across an interface region that is nevertheless localized to the vicinity of the diagonal plane. The actual process of mutual penetration of particles from both sides of the diagonal plane, inherent in the bifurcated flow regime, is determined by the main harmonics superimposed on the base flow, as shown in Fig. 12c, f, i. Particles that cross the diagonal plane due to symmetry breaking are entrained by the prevailing base flow and dispersed throughout the entire cavity. Note that an extensive region with considerable oscillation amplitudes for all three velocity components is also located close to the leading corner of the cavity bottom (see Fig. 6g–i). This explains the enhanced particle intrusion in this area, which is characterized by a twisted plume shape rising from below (see Fig. 12c, f, i).

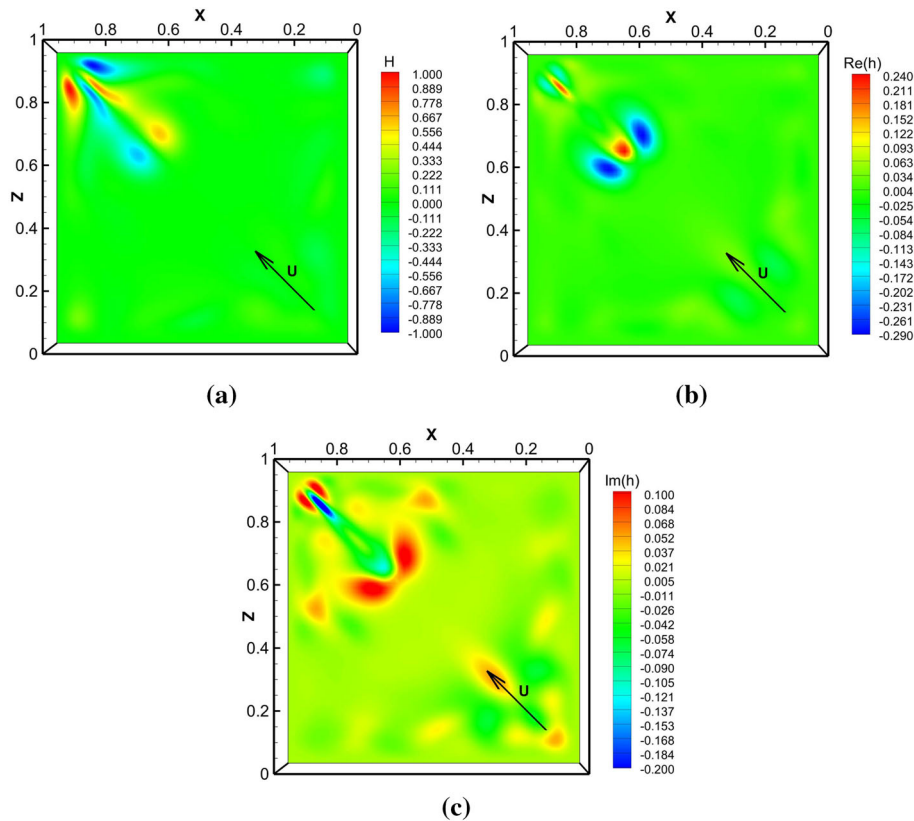


Fig. 11 The spatial distributions of the helicity density corresponding to: **a** the base flow; **b** the real part of the flow main harmonic; **c** the imaginary part of the flow main harmonic. The distribution is presented for the cavity mid-span cross section, $Re = 2335$. The *arrows* indicate the direction of lid movement

3.5 Structure of the internal vortices

Flow vortices inherent in perturbed cavity flows are typically characterized by finite oscillating amplitudes, whereas the cavity end walls have only a very small effect on the flow pattern [42]. The lid-driven cavity flow is therefore a particularly attractive platform for experimental investigation of time-periodic three-dimensional vortices. The complexity of the vortex interactions effected by the presence of nonslip boundaries gives rise to an impressive variety of instabilities and bifurcation scenarios including elliptic, quadripolar, centrifugal and cooperative instabilities [42]. All these instabilities were obtained by exploring the 2D-3D transition in either the “classical” lid-driven cavity or in cavities with parallel/antiparallel wall motion. In this section, we demonstrate that the diagonally lid-driven cavity flow, that is under investigation here, can certainly be considered as an alternative platform for further numerical and experimental investigation of the vortex interactions inherent in highly separated essentially three-dimensional flows.

Figure 13a presents the y (vertical) component of the vorticity distribution of the base flow taken at the cavity mid-span cross section and computed as a curl of the velocity field averaged over a whole number of periods. The representative base flow pathlines projected onto the mid-span plane are superimposed onto the contours. The pattern so obtained can be interpreted as a flow *topographic map*, in which the closed contours determine the size and position of the corresponding vortex cores. Four different vortex groups (marked with numbers 1–4) can be recognized as bearing a striking resemblance to the steady-state flow pattern reported for $Re = 2000$ in [24]. It should be noted that only the counter-rotating vortex pair marked by the number 2 has a clearly distinguishable core of a nearly elliptic shape, whereas all the other vortices exhibit the flow converging to their centers. The base flow vorticity field is antisymmetric and strained close to the diagonal interface plane, where it attains maximum absolute values, similar to that determined in [43] with respect to the stationary elliptic instability of the vortex pair in an open flow.

As already mentioned, given that the flow is determined by only a single oscillating mode with moderate amplitudes, the spatial distribution of eigenvector magnitudes of any flow field can be approximated by the

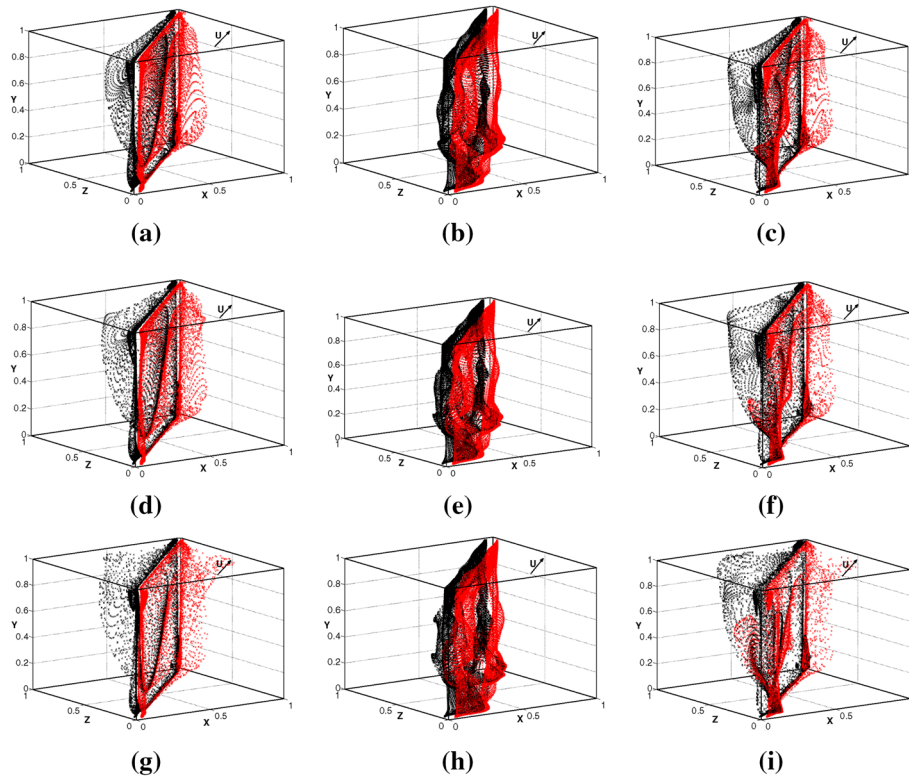


Fig. 12 The temporal distribution of passive particle tracers corresponding to the base flow: (a, d, g); the main flow harmonic: (b, e, h); and the overall bifurcated flow (base flow with superimposed main harmonic). The time evaluations were taken at $t = T/5$: (a-c); $t = T/4$: (d-f); $t = T/3$ (g-i). The arrows indicate the direction of lid movement, $Re = 2335$

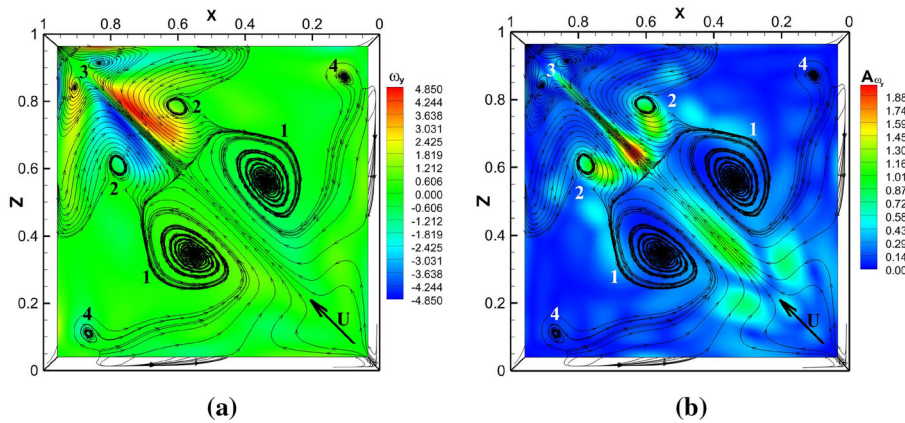


Fig. 13 Base flow path lines projected on a mid-cross section, superimposed with: **a** base flow vorticity field; **b** oscillation amplitudes of the y (vertical) component of the vorticity field. The arrows indicate the direction of lid movement, $Re = 2335$

corresponding oscillation amplitude distribution. Figure 13b presents the reflection symmetric distribution of the averaged oscillation amplitude of the y vorticity component taken at the mid-span cross section. Looking at Fig. 13b, one can recognize an oscillation amplitude peak of ω_y , located on the interface between the two vortices, which is apparently the result of local centrifugal effects of the flow. In this region, the streams symmetrically moving away from the cavity walls meet the oppositely directed stream driven by the cavity lid (see Fig. 13b regions 1, and 2). As a result, both counterflows decelerate while turning downward into the cavity and then each separately proceeds to its cavity part. At the same time, inertia interferes with the flow rotation, originating an instability characterized by increased velocity and vorticity oscillations.

4 Conclusions

Oscillatory instability of the flow inside a diagonally lid-driven cavity was investigated by a series of DNS. It was demonstrated that the DNS approach conducted with a standard second-order accuracy time-marching solver can successfully reveal the main instability characteristics of the three-dimensional highly separated, shear-driven confined flow with all no-slip boundaries. The calculations were performed on two successive stretched grids of 100^3 and 200^3 finite volumes, and Richardson extrapolation was used to approximate the results to the zero-grid-size limit. It was found that the transition to unsteadiness takes place via subcritical Hopf bifurcation at $Re_{cr} = 2320$ and $\omega_{cr} = 0.249$ and is characterized by a spontaneous symmetry breaking of the flow. The value of the critical Re_{cr} number was further verified by flow simulation at $Re = 2310$, taking the steady flow obtained for $Re = 2300$ as the initial condition. The obtained qualitative and quantitative results of the steady-state flow fields were presented.

The bifurcated periodic flow is characterized by reflectional symmetry fields of the velocity base flow and by the oscillation amplitudes of the u_{perp} velocity component. In contrast, the oscillation amplitudes of the u_y and u_{dir} velocity components are antisymmetric. The symmetry-broken instantaneous flow field is characterized by in-phase u_{perp} and out-of-phase u_y and u_{dir} velocity components up to a small offset. The offset is a consequence of the symmetry breaking that results from the u_{perp} velocity oscillations on the interface surface. As the distance to the interface surface decreases, the offset value approaches zero.

A mechanism of the observed oscillatory instability was thoroughly investigated by means of the spatial distribution of the base flow characteristics and oscillating amplitudes, and a Fourier analysis of the main oscillating harmonic and helicity fields of the flow. The flow mixing phenomenon was visualized by tracking the Lagrangian tracers initially seeded from both sides of the diagonal plane of the cavity. The study demonstrated how the DNS approach can be efficiently exploited for a global stability analysis of complex highly separated and previously uninvestigated flows.

Conflict of interest The authors declare that they have no conflict of interest.

References

1. Batchelor, G.K.: On steady laminar flow with closed streamlines at large Reynolds number. *J. Fluid Mech.* **1**, 177–190 (1956)
2. Moffatt, H.K.: Viscous and resistive eddies near a sharp corner. *J. Fluid Mech.* **18**, 1–18 (1963)
3. Kawaguti, M.: Numerical solution of the Navier-Stokes equations for the flow in a two-dimensional cavity. *J. Phys. Soc. Jpn.* **16**, 2307–2315 (1961)
4. Simuni, L.M.: Numerical solution of the problem of the motion of a fluid in a rectangular hole. *J. Appl. Mech. Tech. Phys.* **6**, 106–108 (1965)
5. Shankar, P.N., Deshpande, M.: Mechanics in the driven cavity. *Ann. Rev. Fluid Mech.* **32**, 93–136 (2000)
6. Ertuck, G.: Discussions on driven cavity flow. *Int. J. Numer. Methods Fluids* **60**, 275–294 (2009)
7. Boppana, G., Gajjar, J.: Global flow instability in a lid-driven cavity. *Int. J. Numer. Methods Fluids* **62**, 827–853 (2010)
8. Ramanan, N., Homsy, G.M.: Linear stability of lid-driven cavity flow. *Phys. Fluids* **6**, 2690–2701 (1994)
9. Theofilis, V.: AIAA/CEAS Aeroacoust. Conf. Exhib., 6th, Lahaina, AIAA Paper, pp. 1965–2000 (2000)
10. Ding, Y., Kawahara, M.: Linear stability of incompressible flow using a mixed finite element method. *J. Comput. Phys.* **139**, 243–273 (1998)
11. Albensoeder, S., Kuhlmann, H.: Three-dimensional centrifugal-flow instabilities in the lid-driven cavity problem. *Phys. Fluids* **13**, 121–136 (2001)
12. Feldman, Y., Gelfgat, A.Y.: Oscillatory instability of a three-dimensional lid-driven flow in a cube. *Phys. Fluids* **22**(9), 093602 (2010)
13. Liberzon, A., Feldman, Y., Gelfgat, A.Y.: Experimental observation of the steady-oscillatory transition in a cubic lid-driven cavity. *Phys. Fluids* **23**(8), 084106 (2011)
14. Kuhlmann, H., Albensoeder, S.: Stability of the steady three-dimensional lid-driven flow in a cube and the supercritical flow dynamics. *Phys. Fluids* **26**, 024104 (2014)
15. Natrajam, R., Acrivos, A.: The instability of the steady flow past spheres and disks. *J. Fluid Mech.* **254**, 323–344 (1993)
16. Erikson, L., Rizzi, A.: Computer-aided analysis of the convergence to steady state of discrete approximations to the Euler equations. *J. Comput. Phys.* **57**(1), 90–128 (1985)
17. Gelfgat, A.Y.: Stability of convective flows in cavities: solution of benchmark problems by a low-order finite volume method. *Int. J. Numer. Methods Fluids* **53**(3), 485–506 (2007)
18. Tuckerman, L., Barkley, D.: *Bifurcation Analysis for Timesteppers*. Springer, New York (1999)
19. Giannetti, F., Luchini, P., Marino, L.: Linear stability analysis of three-dimensional lid-driven cavity flow. In: *Atti 19th Congr. AIMETA Mecc. Teor. Appl.*, Ancona, Italy, Art. No. 738. Aras Edizioni, Ancona, Italy (2009)
20. Gómez, F., Gómez, R., Theofilis, V.: On three-dimensional global linear instability analysis of flows with standard aerodynamics codes. *Aeros. Sci. Technol.* **32**(1), 223–234 (2013)

21. Feldman, Y., Gelfgat, A.Y.: From multi- to single-grid CFD on massively parallel computers: numerical experiments on lid-driven flow in a cube using pressure–velocity coupled formulation. *Comput. Fluids* **46**(1), 218–223 (2011)
22. Povitsky, A.: Three-dimensional flow in cavity at yaw. Tech. Rep. 211232, NASA/CR (2001)
23. Povitsky, A.: High-incidence 3-D lid-driven cavity flow. AIAA Paper **2847**, 2001 (2001)
24. Povitsky, A.: Three-dimensional flow in cavity at yaw. *Nonlinear Anal. Theory Methods Appl.* **63**, e1573–e1584 (2005)
25. Yu, D., Mei, R., Luo, L.S., Shyy, W.: Viscous flow computations with the method of lattice Boltzmann equation. *Prog. Aerosp. Sci.* **39**, 329–367 (2003)
26. D’Humières, D., Ginzburg, I., Krafczyk, M., Lallemand, P., Luo, L.S.: Multiple-relaxation-time lattice Boltzmann models in three dimensions. *Philos. Trans. R. Soc. Lond. A* **360**, 437–451 (2012)
27. Freitas, R.K., Henze, A., Meinke, M., Schröder, W.: Analysis of Lattice-Boltzmann methods for internal flows. *Comput. Fluids* **47**, 115–121 (2011)
28. Asinari, P., Ohwada, T., Chiavazzo, E., Di Rienzo, A.F.: Link-wise artificial compressibility method. *J. Comput. Phys.* **231**, 5109–5143 (2012)
29. Weller, H., Tabor, G., Jasak, H., Fureby, C.: A tensorial approach to computational continuum mechanics using object-oriented techniques. *Comput. Phys.* **12**(6), 620–631 (1998)
30. Ferziger, J.H., Perić, M.: *Computational Methods for Fluid Dynamics*. Springer, New York (2002)
31. Drazin, P., Reid, W.: *Hydrodynamic Stability*. Cambridge Mathematical Library, Cambridge (2004)
32. Hassard, B., Kazarinoff, N., Wan, Y.H.: *Theory and applications of Hopf bifurcation*. Mathematics Society Lecture Note Series, vol. 41, London (1981)
33. Kuznetsov, Y.A.: *Elements of Applied Bifurcation Theory*. pp. 273–288. 2nd edn. Springer, New York (1998)
34. Barkley, D., Tuckerman, L.S., Golubitsky, M.: Bifurcation theory for three-dimensional flow wake of a circular cylinder. *Phys. Rev. E* **61**(5), 5247–5252 (2000)
35. Blackburn, H.M., Marques, F., Lopez, J.: Symmetry breaking of two-dimensional time-periodic wakes. *J. Fluid Mech.* **522**, 395–411 (2005)
36. Theofilis, V., Duck, P.W., Owen, J.: Viscous linear stability analysis of rectangular duct and cavity flow. *J. Fluid Mech.* **505**, 249–286 (2005)
37. Moffatt, H.K.: The degree of knottedness of tangled vortex lines. *J. Fluid Mech.* **18**, 117–129 (1969)
38. Moffatt, H.K.: *Magnetic Field Generation in Electrically Conducting Field*. Cambridge University Press, Cambridge (2004)
39. Moffatt, H.K.: Some developments in the theory of turbulence. *J. Fluid Mech.* **106**, 27–47 (1981)
40. Moffatt, H.K., Tsinober, A.: Helicity in laminar and turbulent flow. *Annu. Rev. Fluid Mech.* **24**, 281–312 (1992)
41. Kholmyansky, M., Shapiro-Orot, M., Tsinober, A.: *Proc. R. Soc. Lond. Ser. A* 2699–2717 (2001)
42. Kuhlmann, H., Albensoeder, S.: Strained vortices in driven cavities. *Z. Angew. Math. Mech.* **85**(6), 387–399 (2005)
43. Leweke, T., Williamson, C.H.K.: Cooperative elliptic instability of a vortex pair. *J. Fluid Mech.* **360**, 85–119 (1998)